



ELSEVIER

Available online at www.sciencedirect.com

SCIENCE @ DIRECT®

Journal of Magnetism and Magnetic Materials 267 (2003) 347–356

M Journal of
M magnetism
M and
magnetic
materials

www.elsevier.com/locate/jmmm

Magnetic and structural properties and crystallization behavior of Si-rich FINEMET materials

H. Okumura^{a,*}, D.E. Laughlin^b, M.E. McHenry^b

^aDepartment of Electrical and Computer Engineering, Carnegie Mellon University, 5000 Forbes Avenue, Pittsburgh, PA 15213, USA

^bDepartment of Materials Science and Engineering, Carnegie Mellon University, Pittsburgh, PA 15213, USA

Received 14 March 2003

Abstract

The magnetic and structural properties of an Si-rich grade FINEMET alloy with a composition of $\text{Fe}_{73.5}\text{Si}_{16.1}\text{B}_{6.4}\text{Nb}_{2.9}\text{Cu}_{1.1}$ in at% [$\text{Fe}_{82.7}\text{Si}_{9.1}\text{B}_{1.4}\text{Nb}_{5.4}\text{Cu}_{1.4}$ (wt%)] were investigated after primary and secondary crystallization of ribbon samples. Optimally annealed ribbons exhibited a homogeneous microstructure composed of ~ 7 nm DO_3 nanocrystals surrounded by the retained amorphous phase. This is similar to the base FINEMET. Also, a chemical partitioning model, especially of Si, on slowly heated ribbons above the secondary crystallization temperature ($\sim 700^\circ\text{C}$), is presented herein in conjunction with the reaction products and the magnetic transitions. A self-consistent magnetization analysis is presented which for the first time in FINEMET materials correlates a macroscopic approach from the sample magnetization (using experimentally determined microstructural data such as volume fractions of magnetic phases) with an atomistic approach such as nearest-neighbor calculations and the atomic magnetic dipole moments. The estimated magnetic moment exerted by one Fe atom in the as-spun sample is $\sim 1.67 \mu_{\text{B}}$ on average, while that in a unit cell of the DO_3 phase crystallized from the amorphous is estimated as $\sim 1.85 \mu_{\text{B}}$ per Fe atom ($\sim 24.2 \mu_{\text{B}}$ per a unit cell of the DO_3 phase).

© 2003 Elsevier B.V. All rights reserved.

Keywords: Macroscopic and atomistic magnetization analysis; Chemical partitioning model; Nanocrystallization; FINEMET ribbon

1. Introduction

An $\text{Fe}_{73.5}\text{Si}_{13.5}\text{B}_9\text{Nb}_3\text{Cu}_1$ alloy with a nanocrystalline grain structure, known as FINEMET [1], is an attractive soft magnetic material, which finds use in electric power applications such as transformer cores and other inductive devices. It

exhibits excellent permeability ($\sim 10^5$ at 1 kHz), a low saturation magnetostriction ($\sim 2 \times 10^{-6}$) and a relatively high saturation magnetization (~ 1.2 T). The premier soft magnetic properties are based on the two-phase microstructure consisting of nanocrystalline ferromagnetic grains surrounded by a ferromagnetic amorphous matrix. In order to obtain optimal microstructure and properties, amorphous ribbon precursors produced by melt spinning are generally annealed near 550°C , which is above the primary crystallization temperature of $\sim 510^\circ\text{C}$. The partitioning of glass formers develops to limit the growth of

*Corresponding author. Present address: Department of Socio-Environmental Energy Science, Graduate School of Energy Science, Kyoto University, Sakyo-ku, Kyoto 606-01, Japan. Tel./Fax: +81-75-753-5476.

E-mail address: okumura@energy.kyoto-u.ac.jp
(H. Okumura).

nanometer-sized crystalline (grains) to typically below 10 nm in average size. Since the grain size of the nanocrystalline phase(s) is much smaller than the magnetic *exchange length*, the magnetocrystalline anisotropy and magnetostrictive coefficients are averaged out over the many small grains (as explained by the random anisotropy model) [2]. FINEMET and other nanocomposite magnets have been reviewed recently by McHenry et al. [3].

The early stage of the primary crystallization phenomena involving Cu clustering that leads to the desirable nanoscale microstructure has been intensively studied over the last decade, using techniques that include atom probe field ion microscopy (APFIM), high-resolution electron microscopy (HREM) [4], extended X-ray absorption fine structure (EXAFS) analyses [5] and calorimetric studies [6]. The role of Nb atoms and the mechanism to refine the microstructure has also been studied [5,7]. Different FINEMET grades with higher Fe content to increase the saturation magnetization (up to 1.45 T) were also developed [7]. The change in kinetics of Cu clustering and crystallization in the alloy has been studied [8] regarding the sensitive dependence of soft magnetic properties on Cu content using high-sensitivity differential scanning calorimetry (DSC) and small-angle neutron scattering (SANS). Thus, the structural, calorimetric and extrinsic magnetic properties of FINEMET have been extensively reported, but until now there has been no work on bridging between the magnetic dipole moments (atomistic) and the sample magnetization (macroscopic) in the nanocrystalline/amorphous nanoscale microstructure after primary crystallization. Further, the study on Si-rich grade FINEMET variation is sparse [9,10], and there is no report on the high-temperature crystallization behavior of the alloy (i.e. above the secondary crystallization). These aspects are the subject of this paper.

In this work, we thus report on the magnetic and structural properties and the primary and secondary crystallization reactions of nanocomposite soft magnets with a composition of $\text{Fe}_{73.5}\text{Si}_{16.1}\text{B}_{6.4}\text{Nb}_{2.9}\text{Cu}_{1.1}$ [$\text{Fe}_{82.7}\text{Si}_{9.1}\text{B}_{1.4}\text{Nb}_{5.4}\text{Cu}_{1.4}$ (wt%)] (Si-rich grade FINEMET). This alloy composition is economically advantageous over the base FINEMET composition due to replace-

ment of relatively expensive B by inexpensive Si. Results show that the annealed microstructure at this composition is composed of DO_3 nanograins surrounded by retained amorphous regions as in the base FINEMET alloy, and thus a random anisotropy model is applicable for this system. A chemical partitioning model (especially of Si) is presented for the first time as the observations of the microstructural changes during the secondary crystallization reaction. Also, the macroscopic sample magnetization in FINEMET materials is correlated with reported intrinsic magnetic dipole moments (atomic moments) of Fe atoms through microstructural analyses. They are in good agreement with a reasonably small difference, indicating propriety of the analyses.

2. Experimental

The composition of the initial amorphous precursor FINEMET ribbons was determined using an inductively coupled plasma (ICP) chemical analysis method. Ribbon samples with a thickness of about 20 μm were encapsulated in a quartz tube under argon atmosphere and placed in a preheated furnace for heat treating experiments. X-ray analyses (Cu K_α radiation) were performed using the Rigaku Geigerflex diffractometer with the tube voltage and current of 35 kV and 25 mA, respectively: for a rough scan, divergent slit (DS) of 1° , receiving slit (RS) of 0.3 mm, $0.07^\circ/2 \text{ s/step}$, while for a slow scan, DS of 0.5° , RS of 0.3 mm, $0.015^\circ/5 \text{ sec/step}$ have been used. The magnetic properties at room temperature were measured using a Lake Shore vibrating sample magnetometer (VSM) in an applied field up to 9 kOe, and the $M-T$ (magnetization—temperature) curves were measured using the same VSM equipped with a high-temperature stage, where an applied field of 1 kOe and a heating rate of about 3°C/min were used. The magnetization and the Curie temperature were calibrated using pure nickel and iron samples. JEOL JEM2000-EXII and Philips TECNAI-F20 transmission electron microscopes with energy dispersive spectroscopy (EDS) capability were employed, including high-resolution

microscopy, to study the microstructure and the qualitative composition analyses.

3. Results and discussion

The X-ray diffractometry with a slow step scan on the annealed (550°C for 90 min) ribbons clearly exhibits (inset of Fig. 1) the superlattice reflections from (1 1 1) and (2 0 0) planes of the Fe–Si DO₃ structure. This proves the existence of the DO₃ phase in the heat-treated sample, although the solid solution of BCC-Fe phase with Si may still coexist (the major Bragg peaks of BCC and DO₃ coincide with each other). Both bright field (BF) and dark field (DF) TEM images from the sample exhibit a uniform distribution of grains. Fig. 2(a) shows an example of the DF image, and the grain size distribution shown in Fig. 2(b) is obtained using an image analysis software. A total of 710 grains were examined, and the average size of 6.6 nm was estimated from the log-normal-like distribution. It should be noted that the morphology of the grains appears less spheroidal and less uniform with higher Fe contents.

Fig. 3(a) shows a typical selected area electron diffraction (SAD) image from the sample. When

the diffracted intensity is plotted as a function of $1/d$, the reciprocal of interplanar spacing, the same superlattice reflections as observed in the X-ray results of (1 1 1) and (2 0 0) planes of the DO₃ phase are detected (inset of Fig. 3(b)). Other Bragg peaks again coincide with both the DO₃ and BCC phases, as indexed in the figure. However, as shown later in the magnetic data, most of the particles have the DO₃ structure, and therefore the nanocrystals are designated merely as the DO₃ phase in the remainder of the paper. The lattice parameter of the DO₃ phase is calculated to be 0.566–0.568 nm from the SAD pattern, which is consistent with the X-ray results.

An HREM image of one of the largest particles (the diameter of about 15 nm) displaying the lattice fringes of (2 2 0) DO₃ planes is shown in Fig. 4(a). The d -value of 0.200–0.201 nm is again consistent with both the X-ray results and the above SAD analyses. As shown in Fig. 4(b), there exists at this stage a significant quantity of the amorphous regions often surrounding the ferromagnetic nanocrystals. The boundary between a DO₃ crystal and the amorphous region is shown by arrows in the figure. (The amorphous regions should have different composition(s), especially near the boundary, from the original amorphous regions

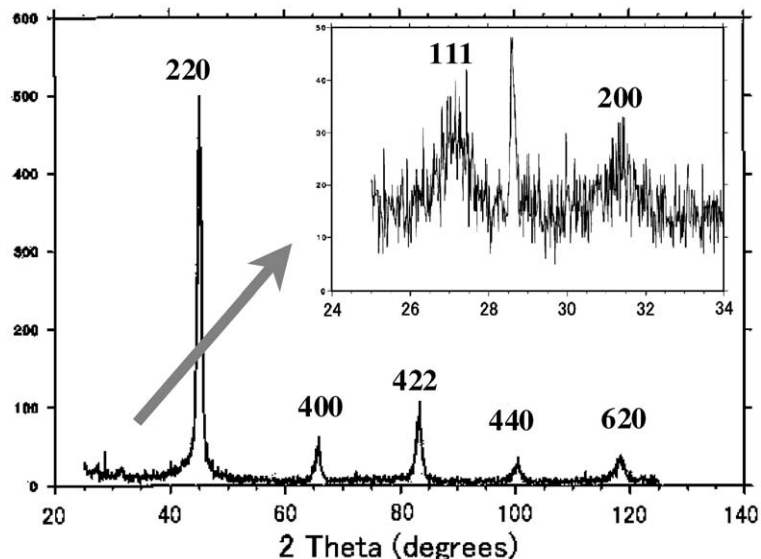


Fig. 1. X-ray diffractometry on annealed (550°C for 90 min) ribbons. Slow step scan (inset) clearly exhibits superlattice reflections of DO₃ phase.

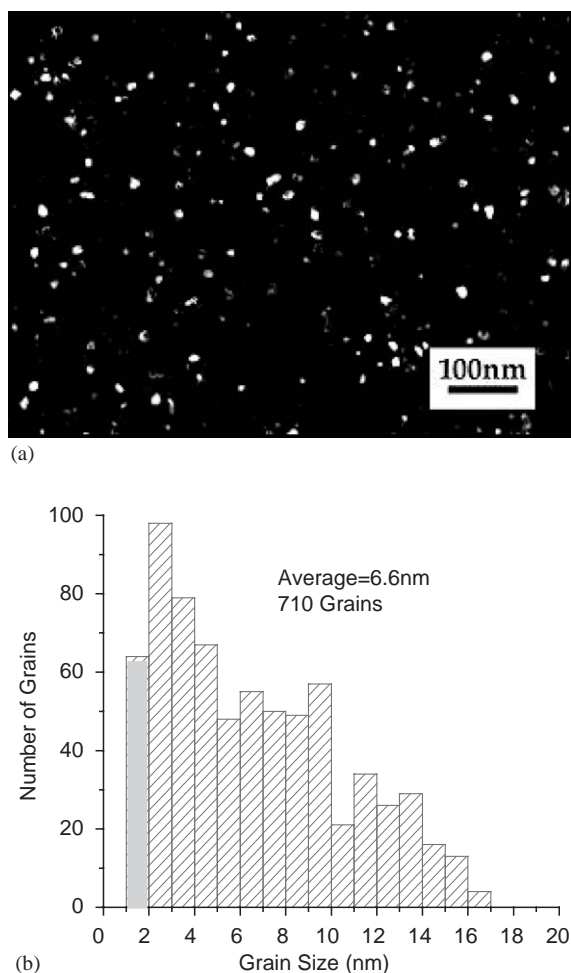


Fig. 2. (a) TEM DF image of annealed (550°C for 90 min) ribbon. (b) Grain size distribution obtained from image (a) using an image analysis software.

due to chemical partitioning during the nanocrystallization process.) Also, from nano-probe EDS analyses, the copper clusters are often enveloped in the DO₃ nanocrystals, indicating that Cu clusters initially form in the amorphous, followed by nucleation and growth of the DO₃ phase on the clusters, as suggested in Ref. [5].

When the amorphous FINEMET ribbon is slowly heated (less than 3°C/min) to 825°C and subsequently slowly cooled to 100°C, the magnetization of the sample changes with temperature as shown in Fig. 5(a). The Curie temperature of the amorphous is estimated by extrapolation to be

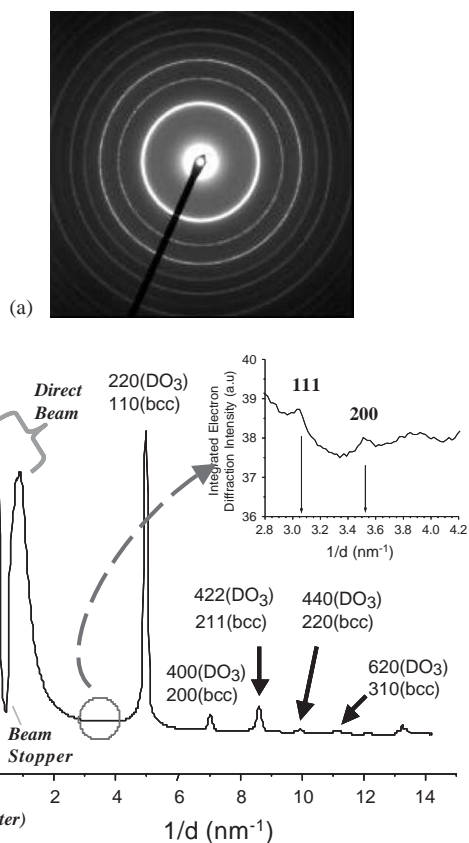


Fig. 3. (a) Electron diffraction image of annealed (550°C for 90 min) ribbon. (b) Diffracted intensity plotted as a function of reciprocal of interplanar spacing.

about 350°C, and the first crystallization from the amorphous starts around 510°C. As shown in Fig. 5(b), if the heating procedure is stopped at 625°C followed by slow cooling of the sample, the cooling curve for the magnetization indicates a curve that can be fitted to a single Brillouin function. Thus, the magnetic phase(s) involved with this reaction is nearly a single phase, and its Curie temperature is estimated to be 625°C. This point is further discussed later, in detail, where we also show that the magnetic phase is DO₃. Also, on the cooling curve after the sample is heated to 825°C (Fig. 5(a)), there are two clear changes in the magnetization, which correspond to magnetic phases with the Curie points about 717°C and ~440°C. As discussed later and also according to the Fe–Si phase diagram (see Fig. 6) [11], the first

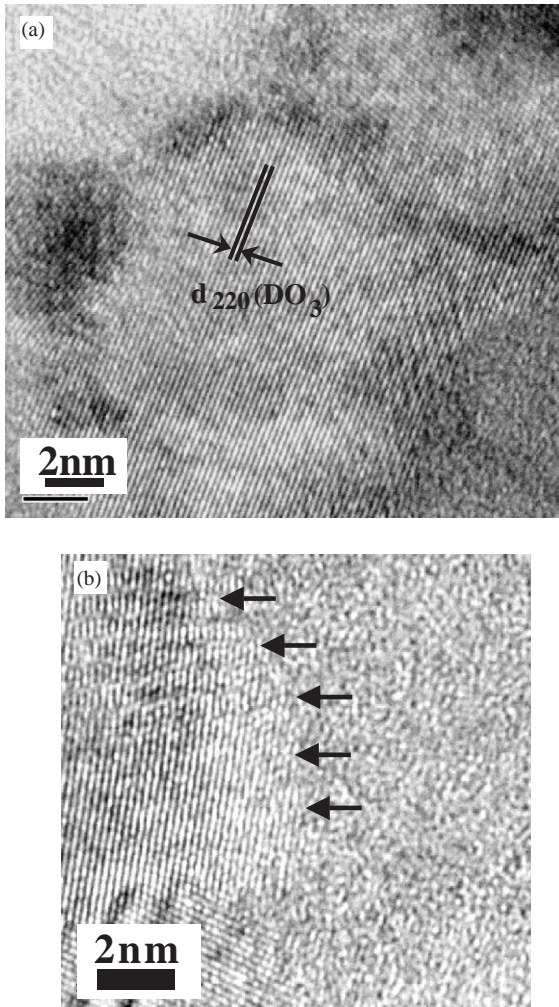


Fig. 4. HREM images of annealed (550°C for 90 min) ribbon. (a) Lattice fringes of (220) DO₃ planes is clearly seen ($d = 0.200\text{--}0.201\text{ nm}$). (b) Amorphous regions often surround ferromagnetic nanocrystals (arrows indicate the boundary).

transition is probably of an Fe–Si solid solution with the BCC (A2) structure, containing ~10.7 at% Si with possible B interstitials. This phase continuously orders to the B2 structure on cooling, possibly followed by a transformation to the equilibrium DO₃ phase through a two-phase region. The second transition (~440°C) is close to this transformation temperature, but the moment increase is not expected in Fe–Si alloys from the ordering transformation. Also, the magnitude of the change would be much smaller than that

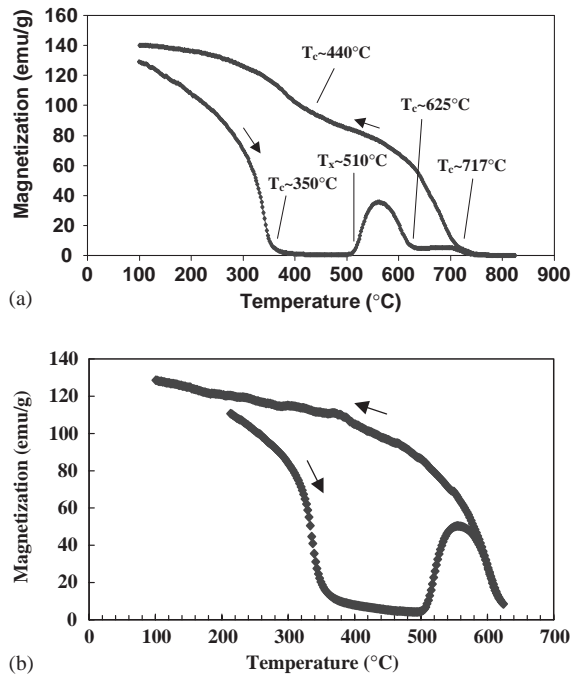


Fig. 5. Variation of magnetization with temperature when (a) the amorphous ribbon is slowly heated (less than 3°C/min) to 825°C and subsequently slowly cooled to 100°C, and (b) the heating procedure is stopped at 625°C followed by slow cooling.

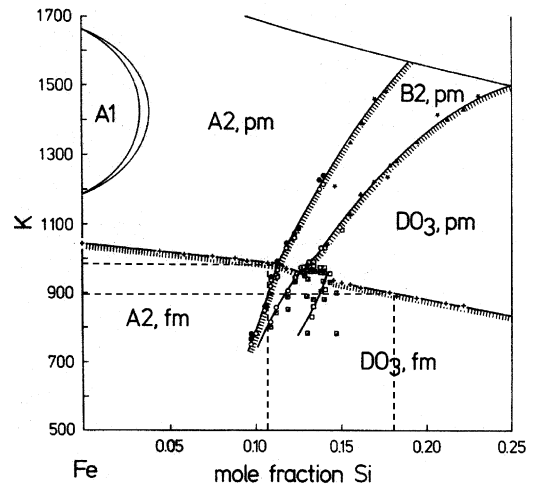


Fig. 6. Fe–Si alloy phase diagram for 0–25 at% Si [11].

observed. In a wide range of Fe–Si–B ternary compositions the amorphous exhibits similar Curie temperatures [12]. Thus, this phase may be

another magnetic phase with a Fe–Si–B ternary composition. This point will be discussed later, but the details are still under investigation.

The room-temperature hysteresis loop of the amorphous ribbon (i.e., the sample state before any heating) is shown in Fig. 7, and displays typical features of a soft magnetic material. The saturation magnetization is estimated from the flat portion to be 138 emu/g (~ 1.3 T). Since the amount of Fe is 82.7 (in wt%), the atomic moment exhibited by one Fe atom is calculated as $1.67 \mu_B$. At this stage, ultrafine nanocrystals (< 2 nm in size) are surrounded by the amorphous matrix, as observed by TEM DF images.

Once the sample is heated to 825°C and cooled to room temperature, which is after the experiment shown in Fig. 5(a), the microstructure is complex with three (or more) phases (see Fig. 8). The large grains, which compose most of the micrographs seen in BF and DF TEM images in Figs. 8(a) and (b), respectively, have the BCC or a BCC-derivative structure (A2, B2 and/or DO_3) as seen from electron diffraction analyses. Provided that the above magnetic analysis about the composition is correct, the volume fraction of this phase can be roughly estimated to be 50–60%. Fig. 8(c) shows a typical SAD pattern, where the strong spots and rings correspond to any of the above phases. From

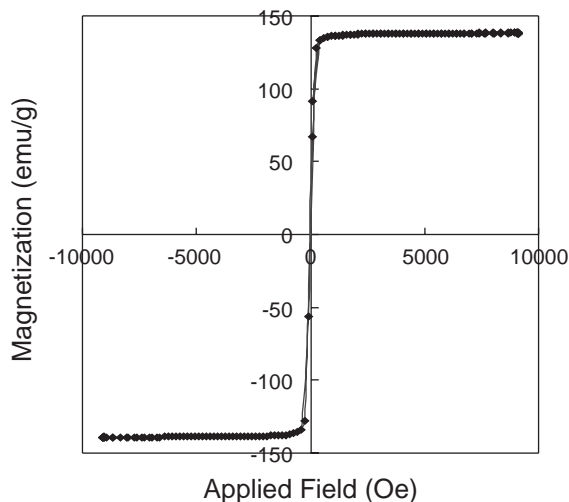


Fig. 7. Room-temperature magnetic hysteresis loop of amorphous ribbon displaying typical features of a soft magnetic material.

the above magnetic data analyses the structure is probably B2 and/or DO_3 . A microbeam diffraction from one of the large grains (as large as 300 nm in size) in the $[0\ 1\ 1]$ zone axis for B2 structure ($[0\ 2\ 2]$ for DO_3) is shown in Fig. 8(d). The possible other minor phases identified from SAD pattern in Fig. 8(c) include $\text{Fe}_{10}\text{Si}_2\text{B}_3$, NbSi_2 , Nb_5Si_3 , Fe_5Si_3 , Fe_{23}B_6 , Nb, Fe_2Nb and NbB_2 . (Complete matching of the Bragg peaks is difficult due to the shift of the peaks caused by some alloying.) Particularly, an Fe–Si–B ternary phase with a composition of, or similar to, $\text{Fe}_{10}\text{Si}_2\text{B}_3$ is a strong candidate since its Curie temperature is $\sim 440^\circ\text{C}$. Thus, it is likely that at higher temperatures (above $\sim 700^\circ\text{C}$) some Si atoms diffuse out of many of the DO_3 grains (with a composition of Fe–18 at%Si) to form Nb silicide(s) and/or Fe_5Si_3 at the grain boundaries replacing retained amorphous. At the same time some grains gain B atoms from the retained amorphous regions to form the Fe–Si–B ternary phase without losing most of their Si atoms. This has to be further investigated to understand the high-temperature reactions in Si-enriched FINE-MET ribbons.

On the other hand, when the heating process is reversed just above the Curie temperature of the DO_3 phase with this composition (i.e. $\sim 625^\circ\text{C}$, see Fig. 5(b)), a homogeneous distribution of DO_3 grains with a grain size of 10–25 nm is obtained. Figs. 9(a) and (b) show the typical BF and DF TEM images, respectively, where the average grain size is 14–15 nm. As clearly seen in the DF image, there are retained amorphous regions at the grain boundaries, which must have a different composition from the original amorphous phase due to chemical partitioning. The electron diffraction pattern in Fig. 9(c) that is taken from a large area clearly exhibits superlattice reflections from the DO_3 phase, not only from low-index planes such as 111 or 200 but also from high-index planes such as 331 or 420, etc. due to the large amount of the highly ordered superstructure. All diffracted intensity positions matched with theoretically calculated Bragg reflections from the DO_3 phase with a lattice parameter of 5.653 \AA .

The composition of the DO_3 phase grains is estimated from the transition temperature to be around Fe–18 at%Si, using the Fe–Si phase

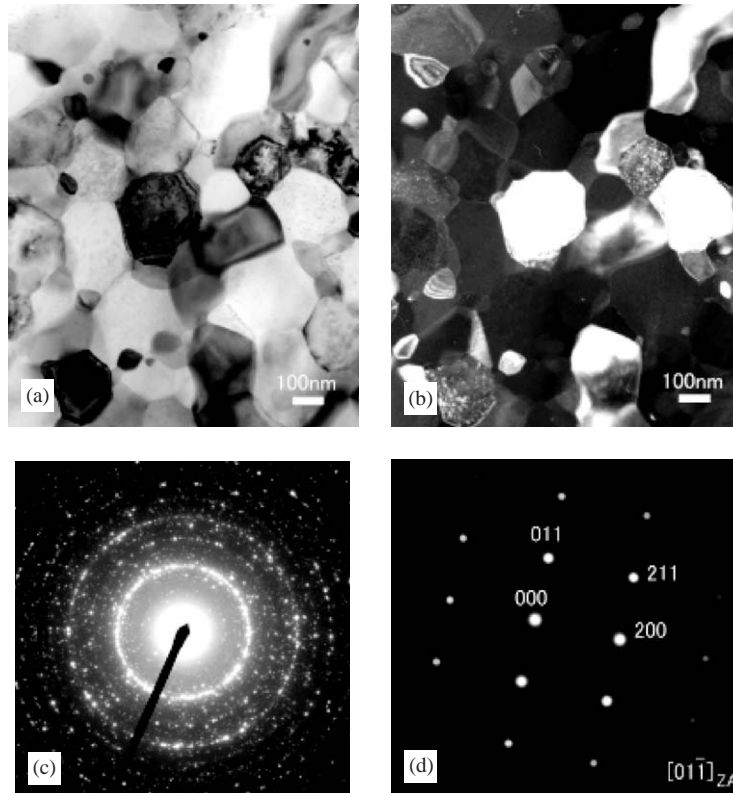


Fig. 8. TEM study on ribbon sample after the experiment shown in Fig. 5(a) (slowly heated to 825°C and cooled to room temperature): (a) BF image, (b) DF image, (c) electron diffraction pattern, and (d) microbeam diffraction from a large grain (~ 300 nm).

diagram of Fig. 6 [11], which is consistent with the original Fe/Si ratio in the amorphous ribbon. The relationship between the Curie temperature and the Si concentration in the Fe–Si phase is known in this system [9]. The composition obtained for the Fe–Si grains is also suggested by the APFIM results [13]. The volume fraction of the DO_3 grains may be estimated using the equation [14]

$$f_{\text{DO}_3} \sim \frac{1}{1 + (3r_0/D) + (24r_0^2/\pi D^2)}, \quad (1)$$

where D signifies the average grain diameter and r_0 the average thickness of the grain boundary phase. By taking D to be 14.5 nm and r_0 as 1–1.4 nm from TEM observations, the volume fraction is found to be 75–80%, which is consistent with two-dimensional estimates of the fraction from the TEM images. Similar volume fraction results have also been reported before [9,15,16]. If this grain

volume fraction with the DO_3 structure is converted to a grain weight fraction, it becomes about 77–82% assuming the grain composition of Fe–18 at%Si.

In the DO_3 structure (16 atoms in a unit cell) with a composition of Fe–25 at%Si (Fig. 10 and Table 1) there are 4 Fe(I) atoms with 8 Fe nearest neighbors (NN), 8 Fe(II) atoms with 4 Fe and 4 Si NN atoms, and 4 Si atoms with 8 Fe NN atoms. However, in a DO_3 phase with 18 at%Si, there are on average 13.12 Fe atoms and 2.88 Si atoms in a unit cell, i.e., 8 out of 9 unit cells have 13 Fe and 3 Si atoms, and 1 out of 9 has 14 Fe and 2 Si atoms. If one Si atom is replaced by an Fe atom from an Fe_3Si unit cell, i.e., 13 Fe atoms and 3 Si atoms in a unit cell, the number of Fe(I) becomes 5 and other 8 Fe atoms now have 5 Fe and 3 Si NN atoms (denoted as Fe(II')). Also, when two Si atoms are replaced (14 Fe and 2 Si atoms in a unit cell),

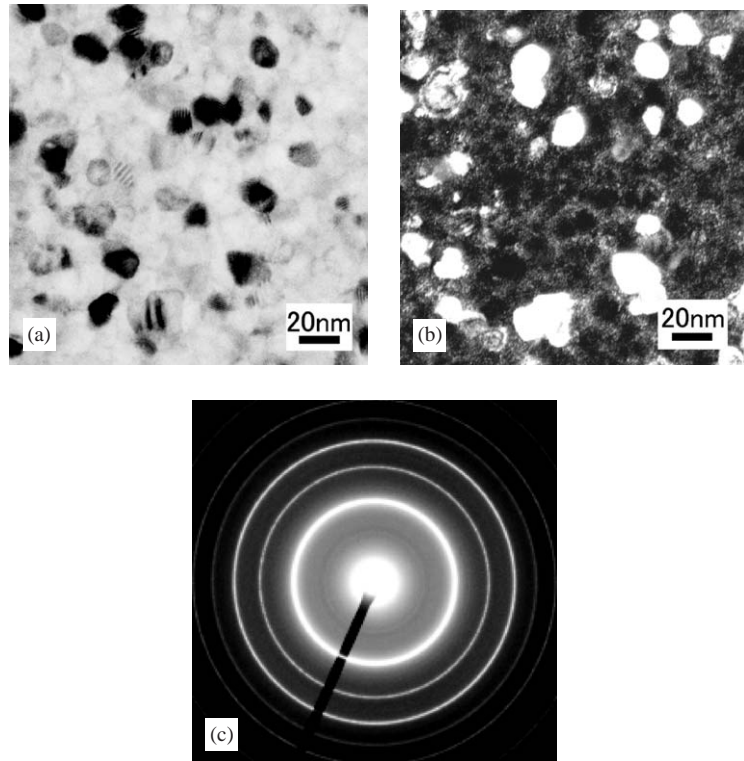


Fig. 9. TEM study on ribbon sample after the experiment shown in Fig. 5(b) (slowly heated to 625°C and cooled to room temperature): (a) BF image, (b) DF image, and (c) electron diffraction pattern.

Table 1

Estimated magnetic moment and nearest neighbor of Fe in a DO_3 phase unit cell based on atomic moment data [17,21,22] at room temperature

DO_3 -phase composition	Number of Fe atoms in DO_3 unit cell	Number of nearest-neighbor atoms		Notation	Expected Fe atomic moment		Estimated moment of DO_3 unit cell	
		Fe	Si		A	B	A	B
Fe_3Si (Fe–25 at% Si)	4	8	0	Fe(I)	2.38	2.15	18.7	17.8
	8	4	4	Fe(II)	1.19	1.15		
$\text{Fe}_{13}\text{Si}_3$ (Fe–18.75 at% Si)	5	8	0	Fe(I)	2.38	2.15	23.8	22.0
	8	5	3	Fe(II')	1.49	1.40		
Fe_7Si_1 (Fe–12.5 at% Si)	6	8	0	Fe(I)	2.38	2.15	28.6	26.1
	8	6	2	Fe(II'')	1.79	1.65		

6 Fe(I) atoms exist in the unit cell and other 8 Fe atoms have 6 Fe and 2 Si NN atoms (denoted as Fe(II'')). Thus, in 9 unit cells with 118 Fe atoms (18 at% Si), there are 46 Fe(I) atoms, 64 Fe(II') atoms and 8 Fe(II'') atoms.

It is usually a good approximation to describe the dipole moment of Fe atoms as varying linearly

with the number of Si NN atoms (Si coordination of an Fe atom) [17]. Thus, the magnetic moment exhibited by a unit cell on average can be estimated for the Fe–18 at% Si DO_3 structure. However, the slope of the curve describing the variation of the local moment with the number of coordination bonds will typically differ from that

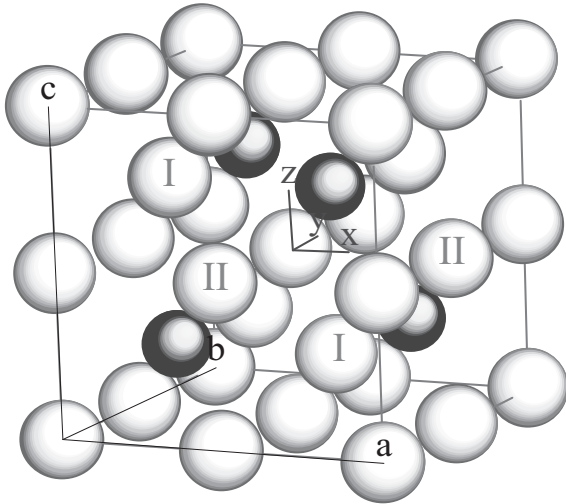


Fig. 10. DO₃ structure with a composition of Fe–25 at% Si (16 atoms in a unit cell). Shaded sphere signifies Si atom, whereas the white sphere signifies Fe atom.

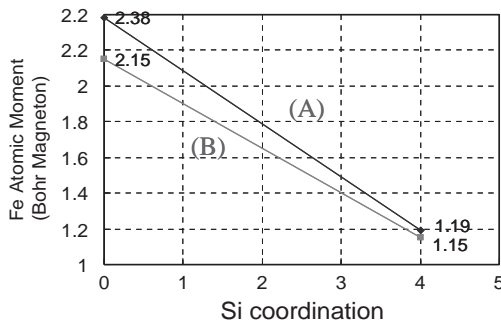


Fig. 11. Linear dilution of Fe atomic moment with Si coordination based on [17,21,22] in Fe–Si alloy.

predicted by simple dilution models due to (1) the bonding of the Fe with the Si and (2) the fact that Fe has both minority and majority spin states at the Fermi level. The details of such effects have been discussed in the coordination bonding models of Corb and O’Handley [18,19] and the magnetic valence models of Malozemoff et al. [20]. While a prediction of the slope for our alloys is beyond the scope of this paper, we emphasize that the linear relationship presumed is not due to simple dilution. By using the data obtained from line (A) [21,22] in Fig. 11 (we approximate the atomic dipole moment of Fe as a linear function of Si

coordination) [23]

$$\begin{aligned} & (2.38 \times 46 + 1.49 \times 64 + 1.79 \times 8)/9 \\ & = 24.4 \text{ or } 1.86 \mu_B \text{ per Fe atom.} \end{aligned}$$

Since the unit cell mass is 1.351×10^{-21} g, the sample moment becomes 167.1 (in emu/g). On the other hand, if the data from line (B) [17] is used, a similar calculation yields $22.4 \mu_B$ for the unit cell, or $1.71 \mu_B$ per an Fe atom, which corresponds to 153.8 emu/g. Similar approach of magnetization calculation based on the Fe nearest neighbors is also reported in the Fe–Si alloy system [24].

From the above-obtained weight fraction of the DO₃ phase, the magnetic moment exerted purely from the DO₃ phase is estimated as $136/\sim 0.8 = 171$ emu/g, assuming the only magnetic phase is the DO₃ phase. This value is larger than that obtained from either data (A) or (B). However, if we reexamine the *M–T* curve in Fig. 5(a), there is actually a small amount of magnetic phase even at the Curie temperature of the DO₃ phase $\sim 625^\circ\text{C}$, which persists above 700°C . Compared with the *M–T* cooling curve, the amount of the magnetic phase at $\sim 625^\circ\text{C}$ may be close to 10% in volume. Upon considering the moment difference between the DO₃ phase and the magnetic phase (the BCC Fe–Si solid solution has a higher moment), the contribution is roughly estimated to be a few percent. Thus, our estimate is in good agreement with the data (A). The estimated magnetic moment exerted by a unit cell of the DO₃ phase is $\sim 24.2 \mu_B$, which corresponds to $\sim 1.85 \mu_B$ per Fe atom.

4. Conclusion

Si-rich grade FINEMET ribbons with a composition of Fe_{73.5}Si_{16.1}B_{6.4}Nb_{2.9}Cu_{1.1} in at% [Fe_{82.7}Si_{9.1}B_{1.4}Nb_{5.4}Cu_{1.4} (wt%)] exhibit the DO₃ structure after optimal annealing. The microstructure is uniform, composed of the DO₃ nanocrystals (the average grain size ~ 7 nm), surrounded by retained amorphous regions, just as in the base FINEMET, and thus a random anisotropy model should be able to be applied to this system. A chemical partitioning model, especially of Si, above the secondary crystallization temperature

($\sim 700^\circ\text{C}$) was presented in conjunction with the reaction products and the magnetic transitions. Self-consistent magnetization analysis was shown in FINEMET materials where a macroscopic approach from a sample magnetization using experimentally determined microstructural data such as volume fractions of magnetic phases is correlated with an atomistic approach such as nearest-neighbor calculations and the atomic moment. The estimated magnetic moment of one Fe atom in the as-spun sample is $\sim 1.67 \mu_{\text{B}}$ on average, while that in a unit cell of the DO_3 phase crystallized from the amorphous is estimated as $\sim 1.85 \mu_{\text{B}}$ per Fe atom.

Acknowledgements

The authors would like to thank F. Johnson and J. McKinley for their help in performing the magnetic measurements. Also, authors would like to thank Magnetics, Division of Spang and Co. for providing ribbons, and the Data Storage Systems Center of Carnegie Mellon University for partial financial support.

References

- [1] Y. Yoshizawa, S. Oguma, K. Yamauchi, *J. Appl. Phys.* 64 (10) (1988) 6044.
- [2] G. Herzer, *IEEE Trans. Magn.* 26 (5) (1990) 1397.
- [3] M.E. McHenry, M.A. Willard, D.E. Laughlin, *Prog. Mater. Sci.* 44 (1999) 291.
- [4] K. Hono, K. Hiraga, Q. Wang, A. Inoue, T. Sakurai, *Acta Metall. Mater.* 40 (9) (1992) 2137.
- [5] J.D. Ayers, V.G. Harris, J.A. Sprague, W.T. Elam, H.N. Jones, *Acta Mater.* 46 (6) (1998) 1861.
- [6] N. Lecaude, J.C. Perron, *Mat. Sci. Eng. A* 226 (1997) 581.
- [7] Y. Yoshizawa, *Mater. Sci. Forum* 307 (1999) 51.
- [8] M. Ohnuma, K. Hono, S. Linderroth, J.S. Pedersen, Y. Yoshizawa, H. Onodera, *Acta Mater.* 48 (2000) 4783.
- [9] Y. Ueda, S. Ikeda, K. Minami, *Mat. Sci. Eng. A181/A182* (1994) 992.
- [10] N. Lecaude, J.C. Perron, *Mater. Sci. Forum* 269–272 (1998) 713.
- [11] G. Inden, *Bull. Alloy Phase Diagrams* 2 (4) (1982) 412.
- [12] F. Luborsky, J.J. Becker, J.L. Walter, H.H. Liebermann, *IEEE Trans. Magn.* 15 (3) (1979) 1146.
- [13] K. Hono, D.H. Ping, M. Ohnuma, H. Onodera, *Acta Mater.* 47 (3) (1999) 997.
- [14] H. Okumura, Ph.D. dissertation, University of Pittsburgh, 1999.
- [15] G. Herzer, *Mat. Sci. Eng. A181/A182* (1994) 876.
- [16] M. Muller, N. Mattern, L. Illgen, *Z. Metallkd.* 82 (H12) (1991) 895.
- [17] T. Shinjo, Y. Nakamura, N. Shikazone, *J. Phys. Soc. Japan* 18 (6) (1963) 797.
- [18] B.W. Corb, R.C. O'Handley, N.J. Grant, *J. Appl. Phys.* 53 (11) (1982) 7728.
- [19] B.W. Corb, *Phys. Rev. B* 31 (4) (1985) 2521.
- [20] A.P. Malozemoff, A.R. Williams, V.L. Moruzzi, *Phys. Rev. B* 29 (4) (1984) 1620.
- [21] A. Paoletti, L. Passari, *Nuovo Cimento* 32 (1) (1964) 25.
- [22] M.B. Stearns, *Phys. Rev.* 168 (2) (1968) 588.
- [23] D. Meinhardt, O. Krisement, *Z. Phys.* 174 (1963) 472.
- [24] W.A. Hines, A.H. Menotti, J.I. Budnick, T.J. Burch, T. Litrenta, V. Niculescu, K. Raj, *Phys. Rev. B* 13 (9) (1976) 4060.